THE ASTROPHYSICAL JOURNAL, 400:248–259, 1992 November 20

SPECTACULAR HERBIG-HARO OBJECTS IN THE CARINA REGION

K. OGURA[1]
Kokugakuin University, Higashi, Shibuya-ku, Tokyo 150, Japan

AND

J. R. WALSH
Space Telescope European Coordinating Facility, European Southern Observatory, Karl-Schwarzschild Strasse 2, D-8046 Garching bei München, Germany
Received 1992 March 4; accepted 1992 April 29

ABSTRACT

A pair of Herbig-Haro (HH) objects, which, however, are probably independent, designated HH 135 and 136, have been discovered in the eastern Carina region from Schmidt plates with an objective prism. Their HH nature has been confirmed by subsequent low-dispersion slit spectroscopy. Narrow-band CCD imaging of the whole region has also been obtained in the red [S II] lines as well as in the adjacent continuum. They are the most distant (2.7 kpc) HH objects found so far, but both are apparently as bright as, and intrinsically far brighter than, HH 1 and 2 in Orion. On account of this a large number of emission lines have been identified, many of which are [Fe II] lines. Particularly noteworthy is the first detection of a few Fe II permitted lines in HH objects. HH 135, whose morphology is similar to that of HH 1, is probably excited by a very luminous *IRAS* point source ($1.4 \times 10^4 L_\odot$), one of the most luminous among known exciting sources of HH objects. HH 136 is elongated, length ~0.6 pc. with a structure composed of 10 knots, and is probably powered by another source. High-dispersion spectroscopy shows that the emission lines from around the suggested HH 136 exciting source have very broad blue and red wings. The gas is accelerated as it recedes from the outflow source and makes two-staged bow shocks; this may be explained either by an episodic outflow activity or by an MHD effect. The counteroutflow of redshifted emission is discernible in the high dispersion spectra. HH 135 and 136 appear to be the result of star formation due to radiative impulsion in a bright-rimmed cloud.

Subject headings: ISM: individual (HH 135, HH 136) — shock waves — stars: pre–main-sequence

1. INTRODUCTION

Eastern Carina is a region rich in interesting objects—prominent H II regions, open clusters, reflection nebulae, dark clouds, planetary nebulae and so on. Here the Carina spiral arm of our Galaxy stretches away nearly along the line of sight. However no Herbig-Haro (HH) objects have previously been found in this region. This paper reports the first detection of HH objects in eastern Carina.

A group of HH objects have been discovered inside the dark cloud D290.4+1.9 (Hartley et al. 1986), which is situated north of an H II region with an imposing bright rim. This H II region is one of many emission nebulae found in eastern Carina. Hoffleit (1953) and Gum (1955) were probably the first to list it in their catalogs of emission nebulae in the southern sky (Hoffleit 54, Gum 36). It also makes the forth concentration of RCW 54 (Rodgers, Campbell, & Whiteoak 1960). Recently it is listed as object 347 in the extensive catalog of southern H II regions compiled by Brand, Blitz, & Wouterloot (1986, hereafter BBW).

BBW 347 is believed to be excited by hot stars in the nearby open cluster Stock 13 (Gum 1955; Graham 1968; Georgelin & Georgelin 1969). This loose cluster is located about 10′ southeast of the bright rim. The distance of the cluster has been estimated as 2900 pc from Walraven five-color and Hβ photoelectric photometry of 11 stars (Graham 1968). 2670 pc from *UBV* photoelectric photometry of 23 stars (Moffat & Vogt 1975), or 2650 pc from UBV photographic photometry of 111 stars (Steppe 1977). We adopt 2700 pc as the distance of Stock 13 and BBW 347.

Here we report the results of optical imaging and spectroscopic investigation of the newly discovered HH objects, designated HH 135 and 136, continuing the last HH number used by Reipurth & Heathcote (1992). The HH objects were discovered during an objective-prism Schmidt survey, and follow-up narrow band CCD imaging and low- and high-dispersion spectroscopy have been performed to reveal the morphology, excitation, shock conditions, and kinematics of the complex.

2. OBSERVATIONS AND REDUCTION

2.1. *Objective-Prism Schmidt Survey*

Two deep objective-prism plates in the red were taken with the 61/91 cm Curtis Schmidt at Cerro Tololo Inter-American Observatory in 1985 March. The field center was at $\alpha = 11^h10^m$, $\delta = -60°30'$ (1950). One employed a 6° objective prism, giving a dispersion of 600 Å mm^{-1} at Hα in the north-south direction, and 130 μm widening was applied. The other used a 4° prism with a dispersion of 400 Å mm^{-1} at Hα in the east-west direction, and no widening was applied. In both observations a hypersensitized IIIa-F plate was combined with an RG 610 filter, isolating the wavelength range of 6100–6900 Å, and the exposure time was 90 minutes each under excellent seeing conditions (~1″).

2.2. *Narrow-Band CCD Imaging*

Direct CCD imaging has been obtained on and off the [S II] 6717+6731 Å lines. Observations were made at the Cassegrain

[1] Visiting Astronomer at Cerro Tololo Inter-American Observatory which is operated by AURA Inc. under contract to the US National Science Foundation.

TABLE 1

JOURNAL OF SPECTROSCOPIC OBSERVATIONS

Date	Object	Exposure Time (s)	Slit P.A.	Mode[a]
1986 Dec 24....	HH 136 knots A to J	1037	34°5	A
	Sky for HH 136	200	34.5	A
1986 Dec 25....	HH 136 knots A to J	600	34.5	B
	HH 135 and HH 136 knot J	1012	50.0	B
1987 Feb 27....	HH 135 and nebulosity b	600	41.8	A
	Nebulosity a	1224	22.1	A

[a] A: AAT + 25 cm camera + 250B grating + IPCS; B: AAT + 82 cm camera + 1200R grating + GEC CCD.

focus (f/13.5) of the 91 cm reflector at Cerro Tololo Inter-American Observatory on 1989 March 11. The GEC number 13 chip (576 × 385 pixels, 209″ × 140″ field) was used in conjunction with two interference filters: CTIO 6737 with the center wavelength $\lambda c = 6738$ Å and the bandwidth (FWHM) $\Delta\lambda = 87$ Å for the [S II] 6717+6731 Å lines, and the other CTIO 6649 with $\lambda c = 6649$ Å and $\Delta\lambda = 78$ Å, which is for an adjacent continuum region, free of any of the bright emission lines found in HH objects. For the [S II] band two frames of 20 minutes exposure each were obtained, and then co-added after bias-subtraction and flat-fielding. For the continuum band, three frames of 10 minutes exposure each were obtained and processed similarly. The sky condition at the time of the observations was excellent with 1″.3 seeing and high transparency.

2.3. *Low- and High-Dispersion Spectroscopy*

Spectroscopic observations were made in the same manner as in our previous papers (e.g. Ogura & Walsh 1991). Table 1 presents a journal of the observations.

Low-dispersion spectroscopy was obtained with the RGO spectrograph (25 cm camera) mounted at the f/8 Cassegrain focus of the Anglo-Australian Telescope (AAT). The 250B grating and the Image Photon Counting System (IPCS) were employed, covering a spectral range of 3500–7000 Å. The slit was 230 μm (1″.5) wide giving a spectral resolution of ~ 7 Å; the slit length was 123″ (2″.3 pixel^{-1}). As the spectrophotometric standard, L745-46A and W485A (Oke 1974) were also observed with a wide slit (600 μm or 4″.4). At the same time a neutral density filter was used in order to prevent the count rate exceeding the nonlinearity threshold of the IPCS. For HH 136 a separate sky exposure was obtained at a position 125″ northwest of the object in a region where the background emission is low and fairly uniform.

Spectroscopy of HH 135 and 136 was made also at higher dispersion, again on the AAT, in order to investigate the profiles of the Hα and [N II] lines. The RGO spectrograph (82 cm camera) was used in conjunction with the 1200R grating (first order) and the GEC CCD as the detector, the spectral coverage being 6530–6600 Å. The 83″ long and 74 μm (0″.5) wide slit gave a resolution of 0.4 Å (20 km s^{-1}).

The slit positions for both the low- and high-dispersion spectroscopy are shown in Figures 2*a* and 2*b*, respectively. Unfortunately, these slit positions are far from optimum with respect to the positions of the knots of the HH objects, since at the time of the spectroscopic observations good images of the complex were not available, and we had to rely on the SERC/ESO atlases: CCD images were obtained only later.

Spectroscopic data were reduced with the *FIGARO* data reduction system in the same manner as in our previous papers (e.g. Ogura & Walsh 1991). Both the low- and high-dispersion data were wavelength-calibrated by comparison spectra of a Cu-Ar lamp. Then the emission from each knot of the objects was isolated by coadding the corresponding channels. To the low-dispersion data we subsequently applied correction for the atmospheric extinction, flux calibration referring to the measurements of the flux standards made each night, and, finally, sky subtraction using the mean sky spectrum of the adjacent region on the slit or the separate sky exposure.

3. RESULTS

3.1. *Objective-Prism Schmidt Spectroscopy—Discovery*

On the objective-prism plates two objects attracted our attention immediately for their complicated and bright images. Both showed up generally double with the unresolved Hα + [N II] 6548 + 6584 Å image and the [S II] 6717+6731 Å image, but, in some knots even triple (on the 4° prism plate) or quadruple (on the 6° prism plate) additionally with the [O I] 6300 and 6363 Å images. Some continuum emission is also discernible. Thus the nebulosities were suspected of being HH objects, and not of being fragments of an H II bright rims, which they look like at first glance on the southern sky atlases. The plates do not show any Hα emission stars in the vicinity.

3.2. *Narrow-Band CCD Imaging and Astrometry*

The [S II] 6717+6731 Å CCD image is reproduced in Figure 1*a* (Plate 2). Figure 1*b* (Plate 2) shows the image in the adjacent continuum around 6649 Å. Figures 2*a* and 2*b* are the logarithmic contour presentations based on these two images.

HH objects have strong [S II] 6717+6731 Å emission but have essentially no (or at most weak) continuum in the red, the exception being those associated tightly with reflection nebulae. Thus we can discriminate HH objects by comparing their images on the [S II] lines and on an adjacent continuum (see Reipurth & Graham 1988 and Ogura 1990). Caution must be taken, however, when we work in or around H II regions, since fragments or bright rims of H II nebulae are also strong [S II] emitters. With this in mind, structures of HH 135 and HH 136 have been singled out as marked in Figure 1*a*. It is interesting to note that the CCD images, in particular the continuum image, of HH 136 give an impression of a helical structure which is somewhat reminiscent of the nebula associated with AG Car (Paresce & Nota 1989).

Accurate astrometry has been performed for these knots through two steps. First, we determined precise coordinates of 24 stars in the CCD frame in the vicinity of the HH objects by referring to 15 SAO stars on the SERC SR Atlas. The XY measuring machine at Kiso Observatory, Japan, was used for the measurement. Then the pixel numbers of each HH knot on the [S II] CCD frame were transformed into the celestial coordinates with respect to those of the 24 stars by means of polynomials of the second order. The final results are given in Table 2, the accuracy being about $\pm 1''$.

3.3. *Low- and High-Dispersion Spectroscopy*

Intense emission-line spectra, rich in forbidden lines which are typical of HH objects, are observed from all the knots in the low-dispersion data for HH 135 and 136. But some spectral differences, particularly in terms of the relative strength of the continuum, are found from knot to knot of HH 136. Among them knots A and B have similar spectra dominated by forbidden line emission, whereas the rest of the knots have a more

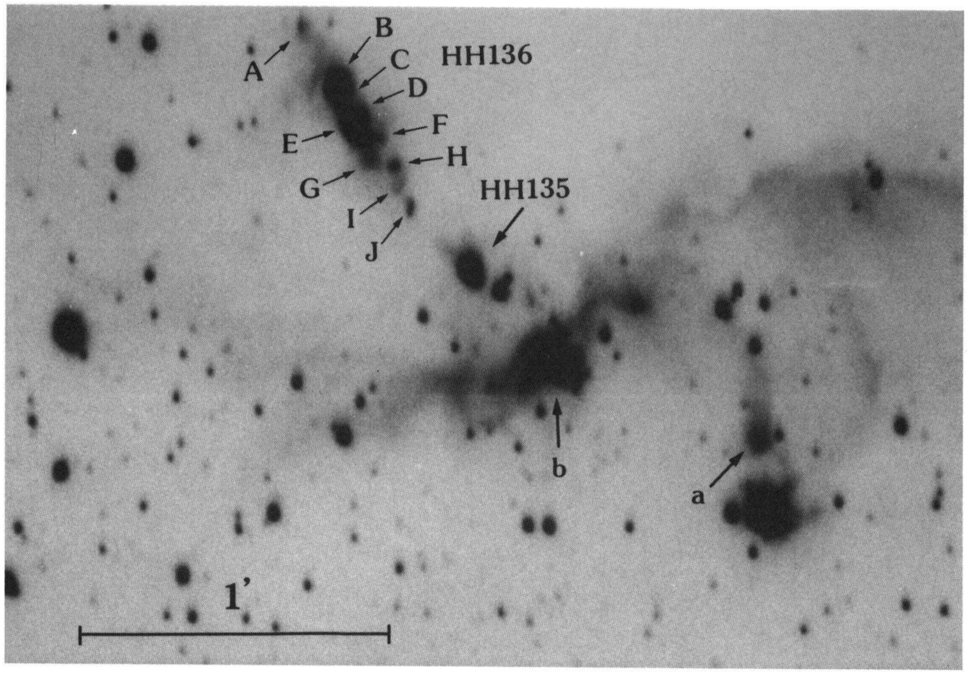

FIG. 1*a*

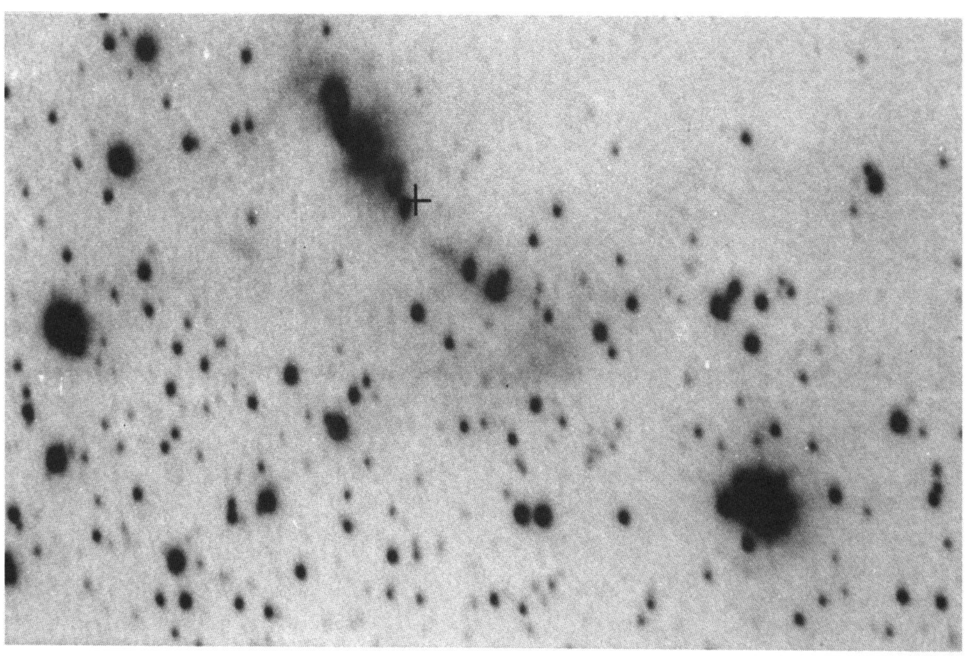

FIG. 1*b*

FIG. 1.—(*a*) Narrow-band CCD image of the region of HH 135 and 136 in the [S II] 6717+6731 Å light. Knots of the HH objects and nearby nebulosities are indicated. The scale is shown. North is up, and east to the left. (*b*) Narrow-band CCD image of the region of HH 135 and 136 in the continuum light around 6648 Å. The cross marks the position of IRAS 11109−5832. The scale is shown. North is up, and east to the left.

OGURA & WALSH (see 400, 249)

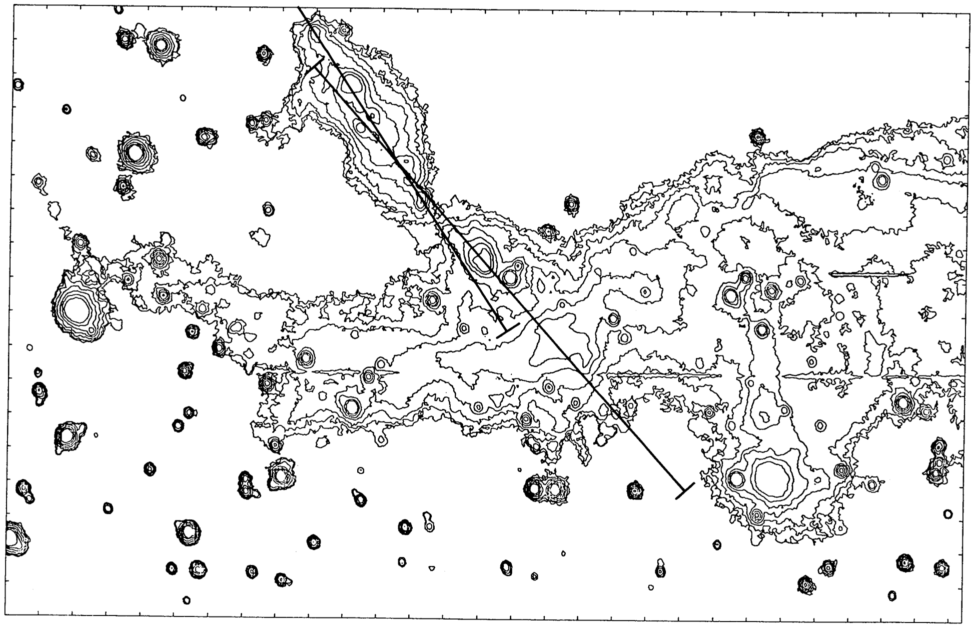

FIG. 2a

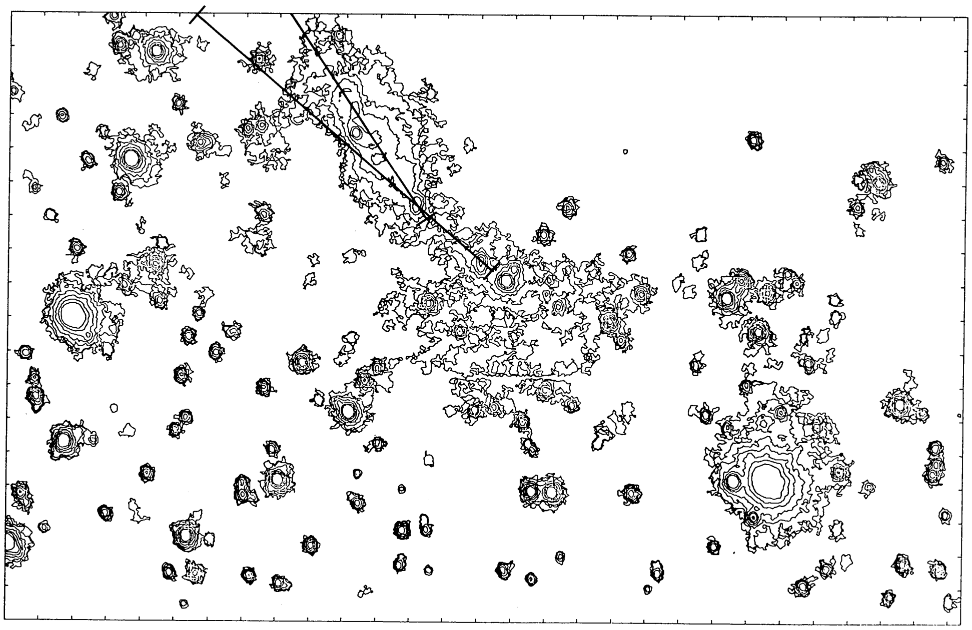

FIG. 2b

FIG. 2.—(a) Logarithmic contour plot of the [S II] image shown in Fig. 1a. The contour levels are 400, 440, 520, 680, 1000, 1640, and 2920 counts. Slit positions of the low-dispersion spectroscopy for HH 135 and 136 are indicated. The field is 3'.4 by 2'.2 wide. North is up, and east to the left. (b) Logarithmic contour plot of the continuum image shown in Fig. 1b. The contour levels are 130, 150, 190, 270, 430, 750, and 1390 counts. Slit positions of the high-dispersion spectroscopy are indicated. The field is 3'.4 by 2'.2 wide. North is up, and east to the left.

or less strong continuum as well as very intense Hα emission. Therefore we show the spectral traces for HH 135, HH 136 knot B and HH 136 knots D/E in Figures 3a–3c, respectively.

In addition to HH 135 and 136, we have obtained low-dispersion spectroscopy for nearby nebulosities which are labeled "a" and "b" in Figure 1a and whose positions are also listed in Table 2. These nebulosities were at first suspected to be HH objects, too. Their spectra are very similar to each other and are of pure emission, dominated by Balmer lines, [O II] 3737+3729 Å and [S II] 6717/6731 Å; forbidden lines characteristic of HH objects, such as [O I] 6300/6363 Å and [N I] 5200 Å, are extremely weak or absent. So, both are low-excitation H II regions and are most probably part of the bright rim.

The emission-line intensities have been derived by Gaussian-fitting for the HH knots and the nebulosities. Tables 3A–3D list all the lines above 3σ level and their relative intensities for HH 135, HH 136 knot A, HH 136 knot B, and nebulosity b, respectively. The errors of the line intensities are estimated from the photon statistics and the continuum fit. For the

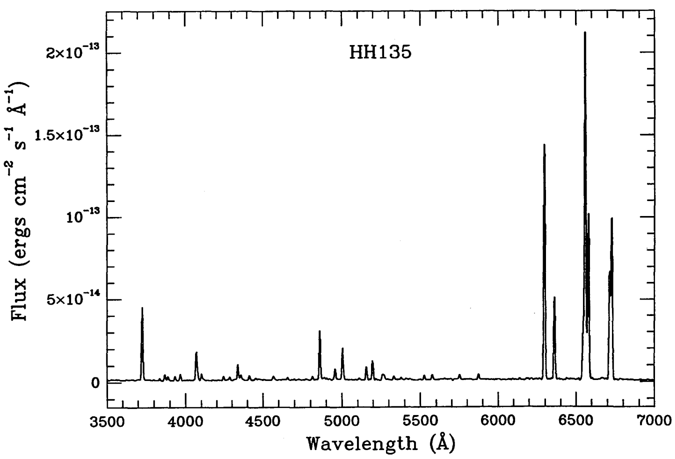

FIG. 3*a*

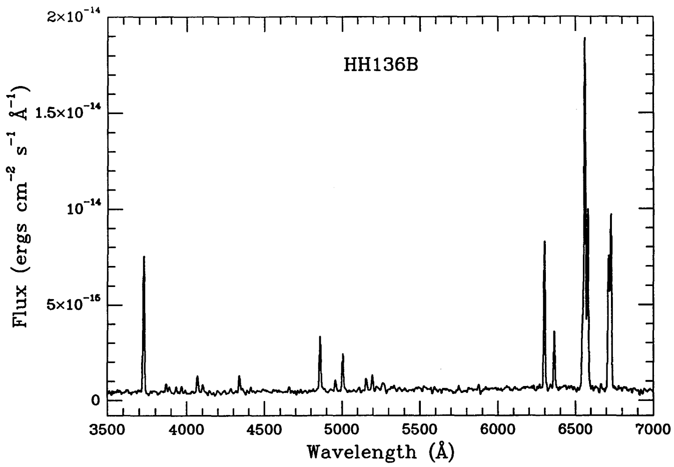

FIG. 3*b*

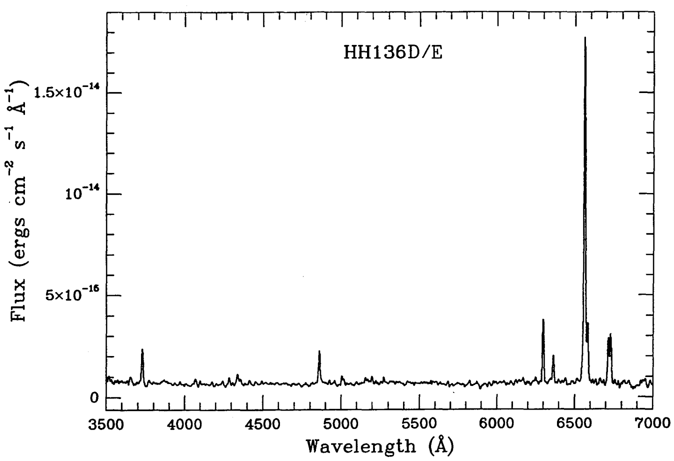

FIG. 3*c*

FIG. 3.—(*a*) Low-dispersion spectrum of HH 135. (*b*) Low-dispersion spectrum of HH 136 knot B. (*c*) Low-dispersion spectrum of around knots D and E of HH 136.

reddening correction we first derived the values of the logarithmic extinction, *c*, at Hβ by comparing the observed Hα to Hβ intensity ratio with the case B recombination value of 2.9 for the temperature 8000 K. Then the observed line intensities are corrected for the selective extinction using the fit by Seaton (1979) to the mean Galactic reddening law with $R = 3.2$. The *c*s and the corresponding values of A_v are given in the lower part of the tables. Also listed there are electron densities N_e, which have been calculated from the [S II] 6717/6731 Å line ratio using the collision strength and transition probabilities tabulated by Mendoza (1983).

There are some sources of limitation in the above analyses. They include (*a*) the use of the case B value of the Hα/Hβ ratio in determining the reddening of the shock excited nebulae, (*b*) the application of Seaton's (1979) reddening curve with $R = 3.2$ in dereddening the line intensities, and (*c*) the possibility that the nebular Balmer lines are contaminated by reflected stellar emission. According to shock models (Shull & McKee 1979; Raymond 1979; Hartigan, Raymond, & Hartmann 1987), the Hα/Hβ ratio can be as high as 4.0, although in most cases it is around 3.0. Therefore our reddening corrections could be overestimates. However, the line intensity of [S II] 10350 Å, which enables Miller's (1968) method to determine the amount of the

TABLE 2

COORDINATES AND EMISSION PROPERTIES OF THE HERBIG-HARO KNOTS AND THE NEARBY *IRAS* POINT SOURCE AND NEBULOSITIES

Object	RA (1950)	Decl. (1950)	Properties
HH 135	$11^h10^m05^s.9$	−58°30′14″	Line emission very strong
HH 136:			
Knot A	11 10 10.7	−58 29 26	Predominantly line emission
Knot B	11 10 09.7	−58 29 37	Predominantly line emission
Knot C	11 10 09.4	−58 29 41	Continuum strong
Knot D	11 10 09.0	−58 29 44	Line emission very strong
Knot E	11 10 09.4	−58 29 47	Continuum very strong, star?
Knot F	11 10 08.5	−58 29 48	Continuum strong
Knot G	11 10 08.8	−58 29 52	Continuum strong
Knot H	11 10 08.1	−58 29 53	Line emission relatively strong
Knot I	11 10 08.0	−58 29 58	Continuum strong
Knot J	11 10 07.7	−58 30 02	Continuum strong
IRAS 11101−5829	11 10 07.4	−58 30 00	
Nebulosity:			
a	11 09 58.1	−58 30 45	H II bright rim
b	11 10 03.6	−58 30 32	H II bright rim

TABLE 3A

EMISSION-LINE FLUXES FOR HH 135

Rest Wavelength (Å)	Line Species	Observed Flux	Error	Dereddened Flux	Error
3502	[Fe II]	1.7	0.5	4.6	1.4
3726/29	[O II]	145.5	2.7	364.4	6.2
3835	H9	3.0	0.5	6.5	1.1
3869	[Ne III]	10.5	0.6	22.2	1.3
3889	H8	7.2	0.6	15.2	1.2
3934	Ca II	7.4	0.6	15.1	1.2
3968/69/70	[Ne III]/Ca II/Hϵ	12.5	0.6	24.8	1.1
4069/76	[S II]	71.0	1.6	131.5	2.9
4102	Hδ	10.9	0.6	19.7	1.2
4115	[Fe II]	3.3	0.4	5.9	0.8
4244	[Fe II]	7.8	0.6	12.7	1.0
4277	[Fe II]	2.0	0.4	3.1	0.6
4287	[Fe II]	6.1	0.5	9.7	0.8
4320	[Fe II]	1.9	0.5	3.0	0.7
4341	Hγ	33.7	1.2	51.0	1.8
4359	[Fe II]	11.3	0.6	16.9	0.9
4414/16	[Fe II]	10.0	0.6	14.3	0.8
4452/58	[Fe II]	5.3	0.5	7.4	0.6
4471	He I	2.6	0.3	3.5	0.4
4479[a]	[Fe II] 4475?	0.9	0.2	1.2	0.3
4489	[Fe II]	2.1	0.4	2.8	0.5
4571	Mg I	9.1	0.5	11.4	0.6
4581	[Cr II]	1.0	0.3	1.3	0.4
4658	[Fe III]	5.0	0.4	5.9	0.5
4686	He II	1.4	0.5	1.6	0.5
4702	[Fe III]	1.7	0.4	1.9	0.4
4728	[Fe II]	2.2	0.5	2.4	0.6
4775	[Fe II]	2.6	0.5	2.8	0.5
4815	[Fe II]	6.8	0.6	7.1	0.6
4861	Hβ	100	—	100	—
4890	[Fe II]	7.0	0.5	6.9	0.4
4905	[Fe II]	2.9	0.4	2.8	0.4
4924	Fe II (42)	2.7	0.5	2.5	0.5
4959	[O III]	23.4	0.9	21.7	0.9
4973	[Fe II]	1.5	0.4	1.4	0.4
5007	[O III]	69.7	1.6	62.0	1.4
5112	[Fe II]	3.4	0.5	2.8	0.4
5158/59	[Fe II]	28.1	1.0	22.1	0.8
5199/5201	[N I]	41.4	1.2	31.6	0.9
5220	[Fe II]	2.7	0.6	2.0	0.4
5262/69/70/73	[Fe II]/[Fe III]	21.6	1.0	15.6	0.7
5334	[Fe II]	7.9	0.7	5.4	0.4
5377	[Fe II]	4.6	0.6	3.1	0.4
5413	[Fe II]	4.3	0.7	2.8	0.5
5527	[Fe II]	8.8	0.7	5.3	0.4
5577	[O I]	9.4	0.8	5.5	0.5
5755	[N II]	11.1	0.8	5.9	0.4
5876	He I	11.2	1.1	5.6	0.6
6300	[O I]	489.7	9.1	195.0	3.6
6364	[O I]	172.1	4.4	66.4	1.7
6548	[N II]	112.4	6.5	39.7	2.3
6563	Hα	793.1	14.9	278.2	5.2
6584	[N II]	372.4	10.1	129.5	3.5
6717	[S II]	243.8	5.8	79.7	1.9
6731	[S II]	372.4	7.8	122.1	2.5
7155	[Fe II]	50.0	2.6	13.6	0.7
7172	[Fe II]	7.7	1.3	2.1	0.4
7292	[Ca II]	41.4	2.5	10.6	0.7
7319/24/30	[O II]/[Ca II]	92.8	3.8	23.6	1.0
7380	[Ni II]	25.5	2.0	6.5	0.5

NOTE.—I (Hβ) = $2.9 \times 10^{-13} \pm 4.2 \times 10^{-15}$ ergs cm^{-2} s^{-1}, $c = 1.46 \pm 0.06$, $A_v = 3.13 \pm 0.13$, $N_e = 3100 \pm 400$ cm^{-3}.

[a] Observed wavelength.

TABLE 3B

Emission-Line Fluxes for HH 136 Knot A

Rest Wavelength (Å)	Line Species	Observed Flux	Error	Dereddened Flux	Error
3726/29	[O II]	451	26	947	54
3869	[Ne III]	17	5	35	10
4069/76	[S II]	27	4	46	8
4102	Hδ	21	4	36	7
4277	[Fe II]	19	5	29	7
4341	Hγ	47	8	67	11
4658	[Fe III]	15	4	18	5
4717[a]	He I 4713?	20	3	22	3
4728	[Fe II]	8	2	9	3
4734	[Fe III]	13	4	15	5
4861	Hβ	100	—	100	—
5007	[O III]	49	9	44	8
5182	[Fe II]	20	5	16	4
5199/5201	[N I]	28	6	22	5
5255[a]	[Fe II] 5262?	24	6	19	5
6300	[O I]	250	15	111	7
6364	[O I]	79	8	34	3
6548	[N II]	118	11	47	5
6563	Hα	723	42	287	17
6584	[N II]	395	25	156	10
6717	[S II]	266	17	99	6
6731	[S II]	225	16	83	6

Note.—I (Hβ) = $8.0 \times 10^{-15} \pm 4.2 \times 10^{-16}$ ergs cm^{-2} s^{-1}, $c = 1.29 \pm 0.19$, $A_v = 2.77 \pm 0.41$, $N_e = 260 \pm 150$ cm^{-3}.

[a] Observed wavelength.

TABLE 3C

Emission-Line Fluxes for HH 136 Knot B

Rest Wavelength (Å)	Line Species	Observed Flux	Error	Dereddened Flux	Error
3726/29	[O II]	236.5	4.9	498.9	10.4
3869	[Ne III[	16.7	1.4	32.6	2.7
3889	H8	11.1	1.3	21.4	2.5
3934	Ca II	10.0	1.4	18.8	2.6
3968/69/70	[Ne III]/Ca II/Hε	11.7	1.2	21.6	2.2
4069/76	[S II]	32.4	1.3	56.1	2.2
4102	Hδ	17.5	1.1	29.7	1.8
4287	[Fe II]	8.3	1.0	12.5	1.4
4341	Hγ	35.5	1.2	51.4	1.7
4359	[Fe II]	3.8	0.7	5.4	1.0
4414/16	[Fe II]	7.0	0.9	9.7	1.2
4493	[Fe II]	8.4	0.8	10.9	1.1
4658	[Fe III]	8.5	0.9	9.8	1.0
4734	[Fe III]	3.9	1.0	4.5	1.2
4861	Hβ	100	—	100	—
4875/81	[Fe II]/[Fe III]	5.9	0.7	5.8	0.7
4890	[Fe II]	3.8	0.7	3.7	0.7
4959	[O III]	20.7	1.0	19.3	1.0
5007	[O III]	64.5	2.0	58.1	1.8
5112	[Fe II]	5.1	0.6	4.3	0.5
5158/59	[Fe II]	24.4	1.3	19.8	1.0
5199/5201	[N I]	29.1	1.3	22.8	1.0
5228[a]	[Cr II] 5224?	11.5	1.2	8.9	1.0
5262	[Fe II]	13.1	0.9	9.9	0.7
5269/70	[Fe II]/[Fe III]	4.4	0.6	3.3	0.4
5273	[Fe II]	9.8	1.0	7.3	0.8
5317	Fe II (48) + Fe II (49)	10.6	1.1	8.0	0.9
5594[a]	?	7.0	1.5	4.3	0.9
5876	He I	9.7	1.7	5.2	0.9
6300	[O I]	259.1	6.6	114.1	3.0
6364	[O I]	104.7	4.3	44.8	1.9
6548	[N II]	125.2	5.0	49.6	2.0
6563	Hα	796.4	14.8	285.9	5.8
6584	[N II]	364.8	8.9	142.4	3.5
6717	[S II]	251.3	11.3	92.9	4.2
6731	[S II]	327.0	11.5	120.2	4.2

Note.—I (Hβ) = $3.2 \times 10^{-14} \pm 5.1 \times 10^{-16}$ ergs cm^{-2} s^{-1}, $c = 1.30 \pm 0.07$, $A_v = 2.79 \pm 0.15$, $N_e = 1400 \pm 300$ cm^{-3}.

[a] Observed wavelength.

TABLE 3D

Emission-Line Fluxes for Nebulosity b

Rest Wavelength (Å)	Line Species	Observed Flux	Error	Dereddened Flux	Error
3726/29	[O II]	229.0	2.8	325.0	4.0
3750	H12	2.6	0.3	3.6	0.5
3771	H11	2.9	0.4	4.1	0.5
3798	H10	4.0	0.3	5.6	0.4
3835	H9	6.3	0.3	8.7	0.4
3889	H8	9.0	0.7	12.2	0.9
3934	Ca II	3.8	0.3	5.1	0.3
3870	Hϵ	13.3	0.4	17.7	0.5
4069/76	[S II]	7.4	0.3	9.6	0.4
4102	Hδ	21.6	0.6	27.7	0.7
4341	Hγ	41.6	0.7	49.5	0.8
4861	Hβ	100	—	100	—
5199/5201	[N I]	7.2	0.4	6.4	0.3
5755	[N II]	2.6	0.7	2.0	0.5
6300	[O I]	21.6	1.1	14.7	0.7
6364	[O I]	6.2	0.8	4.1	0.5
6548	[N II]	81.5	2.7	52.8	1.7
6563	Hα	447.5	6.5	289.0	4.2
6584	[N II]	239.5	4.5	154.0	2.9
6717	[S II]	118.1	3.1	74.0	1.9
6731	[S II]	104.2	2.9	65.2	1.8

Note.—I (Hβ) = $4.8 \times 10^{-13} \pm 4.7 \times 10^{-15}$ ergs cm^{-2} s^{-1}, $c = 0.61 \pm 0.05$, $A_v = 1.31 \pm 0.11$, $N_e = 320 \pm 60$ cm^{-3}.

reddening, is not available in our low-dispersion data. Also we have no information on the R value in this particular region. Given this situation, (*a*) and (*b*) are presumably the most reasonable approximation. As for (*c*), the contribution of the reflected stellar emission does not appear substantial in HH 135, HH 136 knots A and B, and nebulosities a and b, judging from the continuum levels of their low-dispersion spectra as well as from a comparison of Figures 1*a* and 1*b*. But we stopped analyzing the spectra of the rest of the objects where, as mentioned above, the reflection component looks strong.

The high-dispersion spectroscopy has revealed large Hα and [N II] line widths in both HH 135 and 136. In Figures 4*a* and 4*b* (Plate 3) we give the two-dimensional presentation. They show that HH 135 and the northeastern part of HH 136 have highly blueshifted components, whereas the southwestern part of HH 136 exhibits considerably redshifted wings. At the same time it is interesting to note that one finds both the blueshifted and redshifted wings near the center (knots D and E) of HH 136. Figures 5*a*–5*f* show one-dimensional spectra (background-subtracted) for six of the knots (HH 135 and five from HH 136). The Hα profiles of these spectra have been fitted by the minimum number of Gaussians needed to simulate them. The residuals on the observed minus fitted profiles were similar to the photon noise on the observed profiles. The results of the fits, in terms of LSR velocity, FWHM, and relative flux of each fitted Gaussian, are listed in Table 4. The [N II] 6548 + 6584 Å lines give similar results in most cases, but the errors of the fits are larger, since the lines are much weaker than Hα.

4. DISCUSSION

4.1. *Properties of the HH objects*

The first point on which we are impressed by the two HH objects is their remarkable brightness. Our narrow-band CCD images have not been calibrated, but the low-dispersion spectra give the Hβ flux as 2.9×10^{-13} ergs s^{-1} cm^{-2} for HH 135 and 3.2×10^{-14} ergs s^{-1} cm^{-2} for HH 136 knot B. These values compare well with those of HH 1 and 2 in Orion (see Brugel, Böhm, & Mannery 1981). But, contrary to the case of HH 1 and 2, they do not include the flux from the part of the

TABLE 4

Results of Fitting Gaussians to Background-subtracted Hα Profiles of HH 135 and 136

Position	LSR Velocity (km s^{-1})	FWHM (km s^{-1})	Relative Flux
HH 135	−114	112	31
	−33	99	66
	+84	102	3
HH 136 A	−219	87	28
	−119	81	31
	−39	62	41
HH 136 B	−134	98	40
	−50	79	39
	−17	325	14
	+28	64	8
HH 136 D/E	−116	125	20
	−52	61	20
	−15	332	33
	+25	46	20
	+82	76	8
HH 136 G	−110	77	7
	−44	69	18
	+19	477	51
	+28	55	13
	+88	110	12
HH 136 I	+10	142	36
	+32	474	64

Notes.—FWHM corrected for instrumental resolution of 20 km s^{-1}. Background emission has LSR velocity of −18 km s^{-1} and FWHM of 41 km s^{-1}.

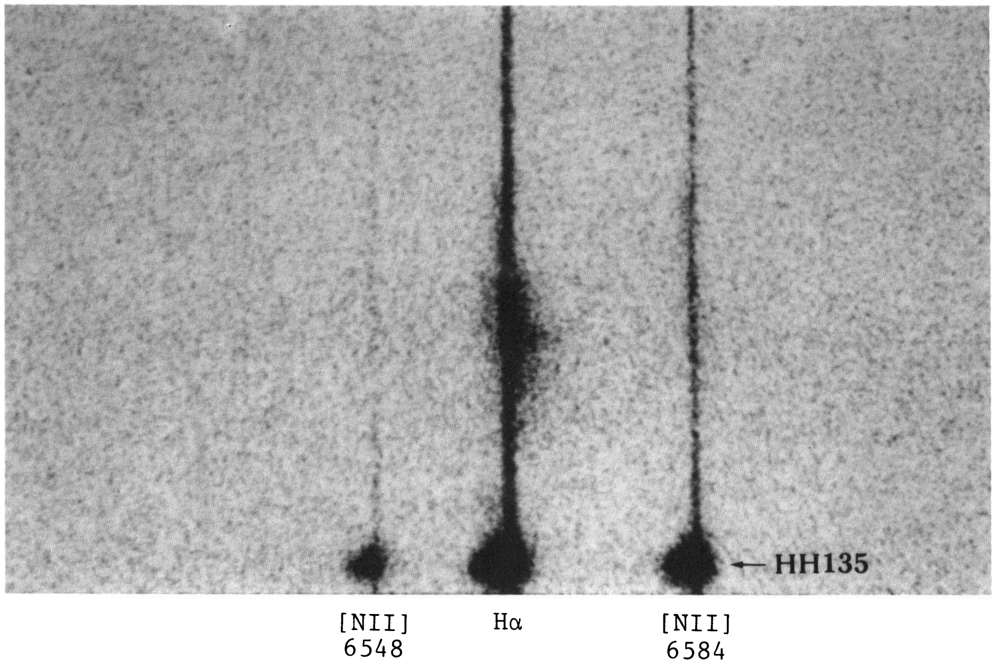

FIG. 4*a*

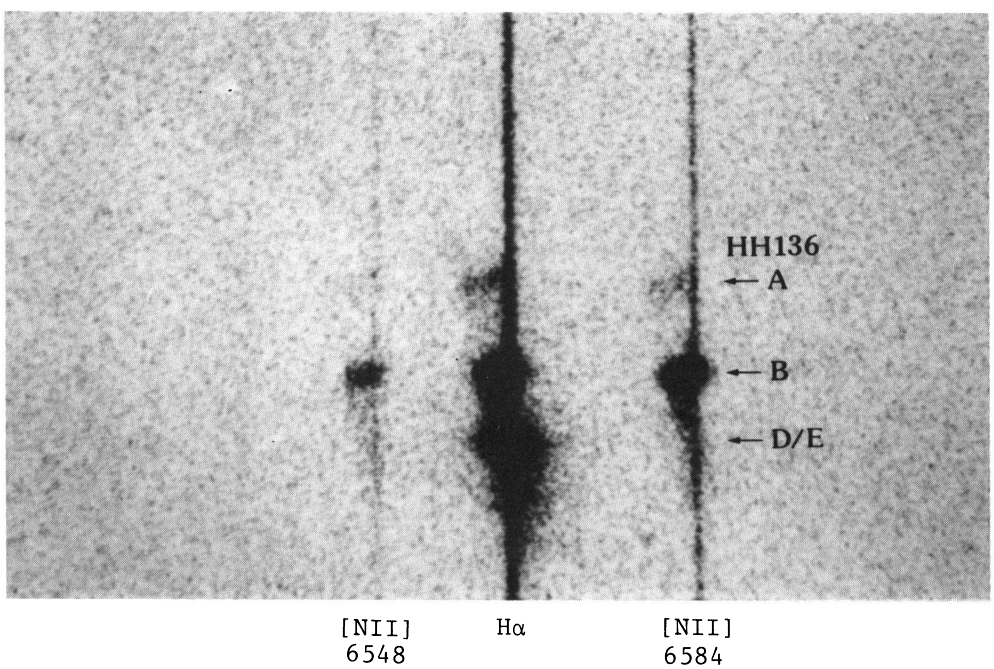

FIG. 4*b*

FIG. 4.—(*a*) Two-dimensional, gray-scale presentation of the high-dispersion spectrum of HH 135 and the southeasten periphery of HH 136 at P.A. 50°. The slit length is 83″. The line identifications and the designation of the HH knots are shown. (*b*) Two-dimensional, gray-scale plot of the high-dispersion spectrum of HH 136 at P.A. = 34°.5. The slit length is 83″. The line identifications and the designation of the HH knots are shown.

OGURA & WALSH (see 400, 254)

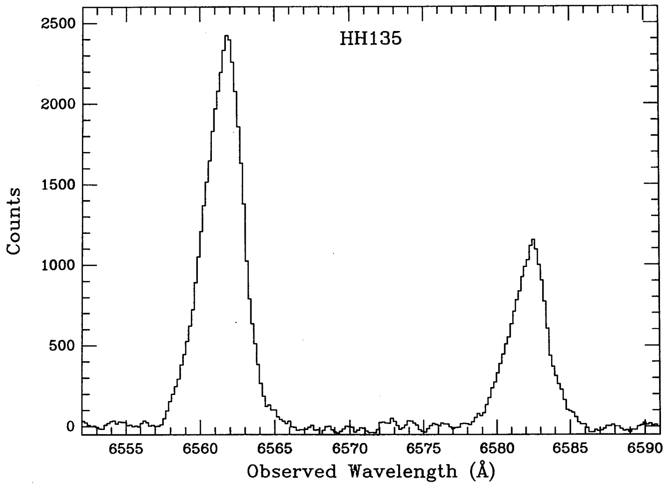

FIG. 5*a*

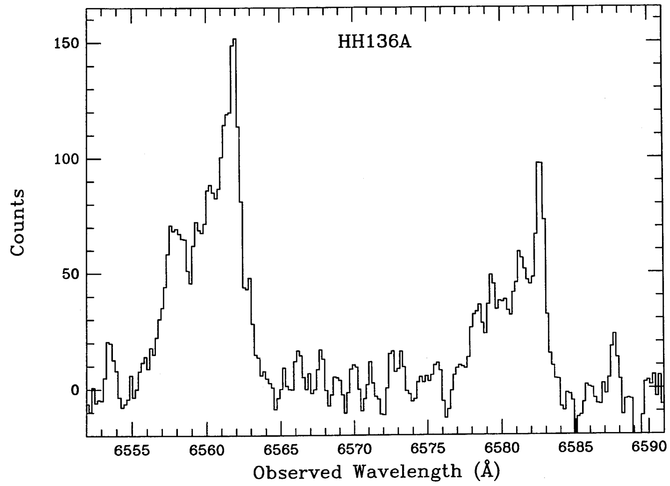

FIG. 5*b*

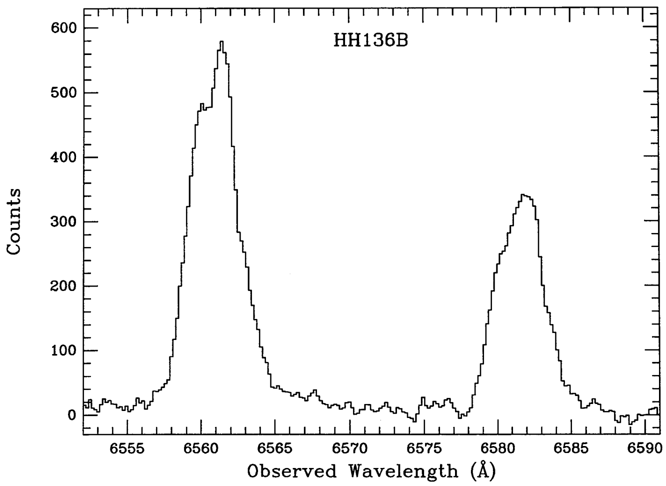

FIG. 5*c*

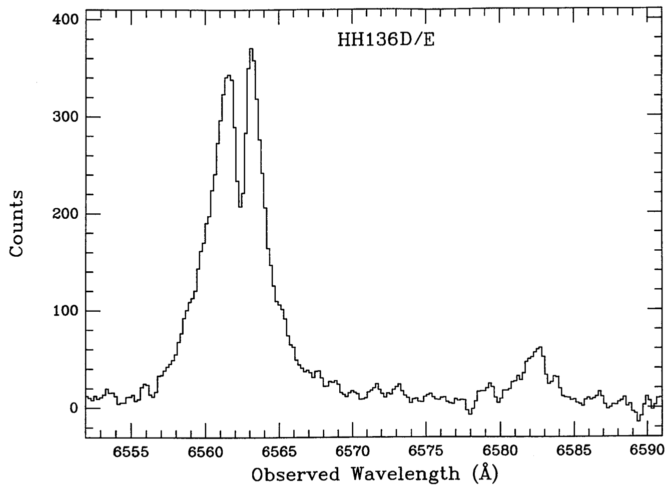

FIG. 5*d*

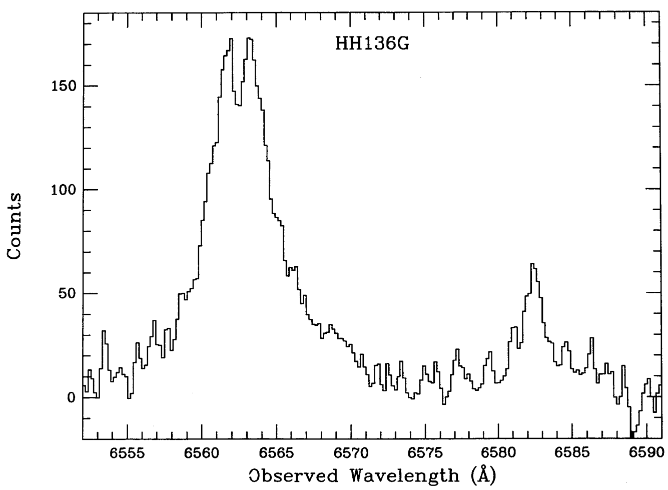

FIG. 5*e*

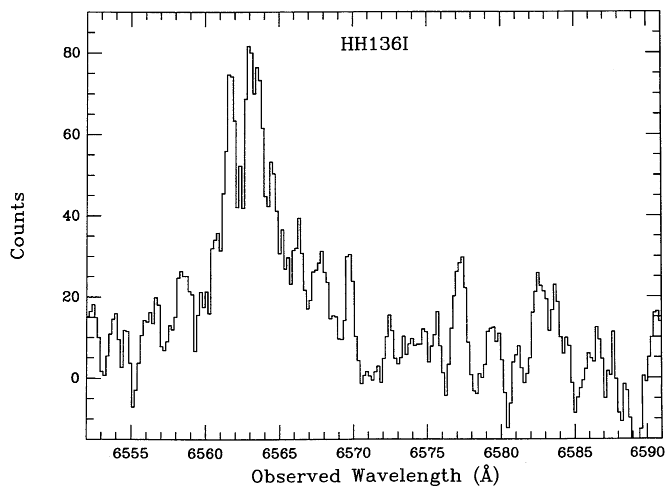

FIG. 5*f*

FIG. 5.—(*a*) High-dispersion spectrum around Hα and [N II] 6584 Å. They are all extracted from the long-slit data with the mean local background emission subtracted. (*a*) HH 135. (*b*) HH 136 knot A. (*c*) HH 136 knot B. (*d*) HH 136 knots D/E. (*e*) HH 136 knot G. (*f*) HH 136 knot I.

objects that is out of the slit entrance. So the total flux can be 5×10^{-13} ergs s^{-1} cm^{-2} for HH 135 and 8×10^{-14} ergs s^{-1} cm^{-2} for HH 136 knot B. The high apparent brightness is all the more remarkable when one considers that HH 135 and 136 are at the distance of 2.7 kpc. They are by far the most distant among known HH objects, the second being 1.5 kpc of HH 72 (Reipurth & Graham 1988) and the Z CMa optical jet (Poetzel, Mundt, & Ray 1989). Taking the flux, the distance and the interstellar extinction into account, we obtain 3×10^{34} and 4×10^{33} ergs s^{-1} as the total Hβ flux of HH 135 and HH 136 knot B, respectively. These fluxes are two to three orders of magnitude higher than that of HH 1 (1.65×10^{31} ergs s^{-1}; Brugel et al. 1981). Thus, being more luminous than HH 80 and 81 (Reipurth 1989c), HH 135 and 136 are the most luminous HH objects known so far.

Because of the high brightness of both HH objects, a wealth of emission lines is observed in the low-dispersion spectra. In HH 135 55 emission lines have been detected, of which 27 are low-excitation forbidden lines of Fe ions. The detected ionization stages range from Mg I (the ionization energy is ~7.6 eV) to He II, O III, and Ne III. Particularly noteworthy is the first detection of permitted Fe II lines in HH objects: Fe II (42) 4924 Å in HH 135 and Fe II (48) + Fe II (49) 5317 Å in HH 136 knot B. Fe II (42) 4924 Å may be blended with He I 4922 Å, but its contribution must not be dominant (see Thackeray 1967). Solf, Bohm, & Raga (1988) failed to detect permitted Fe II lines in their excellent low-dispersion spectra of HH 1, although a large number of Fe II forbidden lines were identified. They concluded that the kinetic energy of electrons is sufficient to excite Fe II forbidden lines (whose excitation energies are ≤ 3.95 eV) but insufficient to excite any permitted Fe II lines (excitation energy ≥ 5.2 eV). The excitation energy of Fe II (42) 4924 Å, Fe II (48) 5317 Å, and Fe II (49) 5317 Å are 5.39, 5.53, and 5.46 eV, respectively, HH 135 and HH 136 knot B are of somewhat higher excitation than HH 1, judging from the intensities of the [O III] lines. This may explain the presence of the Fe II permitted lines in them. Other knots of HH 136 also belong to the class of high excitation HH objects.

Nebulosities a and b have similar amounts of interstellar extinction ($A_v = 1.18$ for a and 1.31 for b). On the other hand, HH 135 and HH 136 suffer heavier extinction ($A_v = 2.8$–3.1; see Tables 3A–3C). The contrast is particularly sharp between HH 135 and nebulosity b which are spatially nearby each other. Presumably the extinction of the nebulosities is caused in the general interstellar space between the Sun and the H II region BBW 347, while the HH objects are partially embedded in the dark cloud D290.4+1.9, which creates the additional extinction. Very noteworthy is the location of the HH objects with respect to the H II region. Recently, it has been established that small dark clouds surrounded by a curved bright rim are sites of active star formation (Sugitani, Fukui, & Ogura 1991). The combination of HH 135 and 136, D290.4+1.9, and the BBW 347 bright rim is one of the best examples of this phenomenon.

Figure 6 shows the Ne-Te forbidden line diagnostic diagram for HH 135, the HH knot with the highest signal-to-noise spectrum, resulting from plots of the line ratio of [O I], [O II], [N II], and [S II]. This can be compared with those for HH 1 and 2, for example, by Brugel et al. (1981). There is an intersection point at $T_e \sim 9000$ K and $N_e \sim 2000$ cm^{-3} and another intersection at higher temperature and density $T_e \sim 15{,}000$ K and $N_e \sim 10^4$ cm^{-3} (from the [S II] (4068+4076)/(6717+6731) Å and [N II] (6548+6584)/5755 Å intersection). The presence

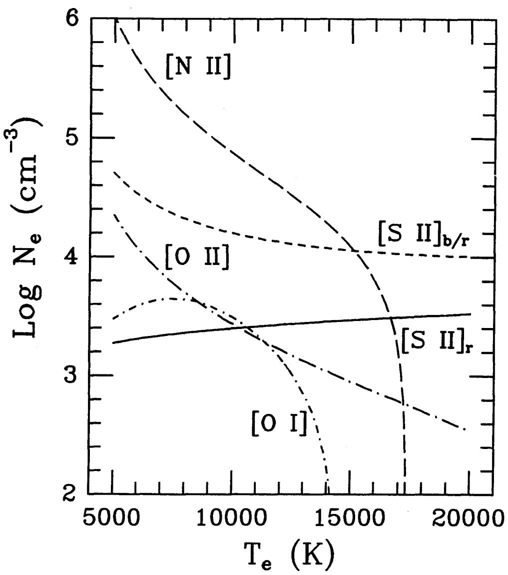

FIG. 6.—Ne-Te diagnostic diagram for HH 135. The loci for the dereddened line ratios of [N II] (6548+6584)/5755 Å, [O I] (6300+6364)/5577 Å, [O II] 3727/7325 Å, [S II] (4069+4076)/(6717+6731) Å (shown as [S II]b/r), and [S II] 6717/6731 Å (shown as [S II]r) are indicated.

of a two-phase medium is quite typical of the spectra of HH objects (see, e.g., Brugel, et al. 1981), although in this case there is a strong difference in their temperature. The [O I] ratio is probably affected by the difficulties of sky subtraction of the airglow line from the faint 5577 Å line, and [S II] (4068+4076)/(6717+6731) Å line ratio is sensitive to reddening. If the reddening were lower than implied by the assumption of case B for the hydrogen lines, then the [S II] ratio would indicate a lower density. It is interesting to note that the spectrum of nebulosity a shows an [N II] (6548+6584)/5755 Å line ratio of 111 ± 23, indicating a T_e of 9000 ± 700 K for $N_e = 150$ cm^{-3}, very different for the [N II] temperature for HH 135, but similar to the indicated temperature of its lower density medium. The lower density gas in HH 135 may be shock compressed local gas which has already cooled and recombined behind the shock and is heated by the local interstellar radiation field. The hotter gas must be much closer to the shock and has not had time to cool appreciably. In terms of bow shocks the hot, dense gas is at the head of the bow shock, while the cooler, lower density gas is in the tail.

4.2. *Do HH 135 and 136 Make an HH Pair?*

Several factors suggest that HH 135 and 136 are not independent and the whole complex makes a single HH pair in such a way as HH 1 and 2 (Herbig & Jones 1981) or HH 46/47 and HH 47C (Graham & Elias 1983; Reipurth & Heathcote 1991), which are excited by a common energy source and moving away in opposite directions. First, HH 135 and the whole HH 136 stand nearly in a straight line (P.A. ~35°). Second, the two brightest parts of them, HH 135 itself and knot B of HH 136 make each other's mirror images morphologically—both have a bow shock–like structure very similar to HH 1. Also their low-dispersion spectra are again alike (see Figs. 3*a* and 3*b*).

However, looking at the high-dispersion data which are outlined in § 3.3, one realizes that HH 135 and 136 are not an HH pair. As is shown in Figures 4*a* and 4*b* as well as Figures 5*a* and 5*c*, both HH 135 and HH 136 knot B have strong blueshifted components. The highest velocity Gaussian component (see Table 4) and the edge velocity of the wing (see Figs. 5*a* and 5*c*) are −114 and −200 km s^{-1} in HH 135, and −134 and −250 km s^{-1} in HH 136 knot B, respectively. These values are so high that no ad hoc explanation is viable to maintain the single outflow hypothesis. For example, the geometrical effect due to flow bent would require a bending angle of 49° for an assumed flow velocity of 300 km s^{-1}. Another fact which supports the idea of the two independent HH objects is that there is a region of predominantly redshifted emission between HH 135 and HH 136 knots A and B. This is shown in Figure 4*b* and, somewhat more clearly, in Figure 4*a* (between about 25″ and 40″ from HH 135 along the slit) whose slit passes the southern periphery of HH 136 knot G. The situation is better illustrated in Figure 7, where we have plotted the Gaussian components of each knot given in Table 4 as a function of its relative position. The size of each dot represents the relative flux of the component, and the bar length the FWHM. The arrowed component is the radial velocity of the local background emission. Clearly the dominant components change their velocities from the highest negative value at HH 136 knot A through practically zero around HH 136 knots D/E to positive values around HH 136 knots G and I, then recover the negative value at HH 135. Thus we conclude that HH 135 and HH 136 are independent HH objects excited by different energy sources.

Does the redshifted gas discussed above correspond to the counteroutflow of HH 136 knots A to C, or of HH 135? Of course the morphology shown in Figures 1*a* and 1*b* favors the former; the portion in question makes a continuation from the northeastern part (knots A to E) of HH 136 in both the [S II] and continuum light. But, as discussed in the following subsection, HH 136 knot J is very close to the energy source of HH 135. Figure 4*b* indicates that the redshifted emission is tightly connected to the redshifted wing of HH 136 knots D/E. Further, Figures 5*d*–5*f* show that HH 135 knots D/E, G, and I have a P Cygni–like profile in Hα in common. So it is concluded that the southwestern part of HH 136 dominated by redshifted emission corresponds to the counteroutflow of its northeastern part rather than that of HH 135.

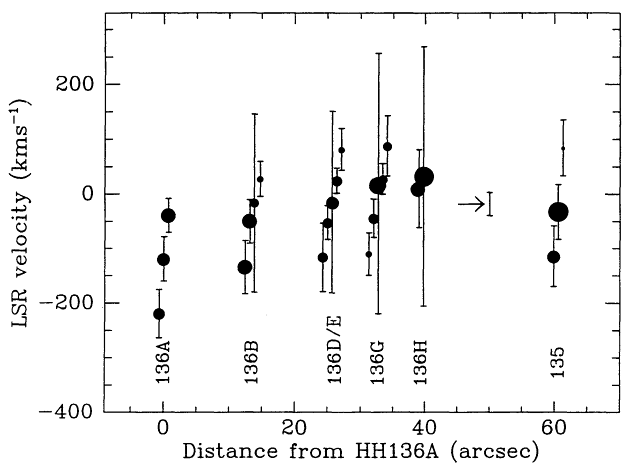

FIG. 7.—Plot of Gaussian components of each knot as a function of its distance from HH 136 knot A. The sizes of dots and the lengths of bars represent the relative fluxes and FWHMs of the components, respectively. The arrowed component refers to the local background emission.

4.3. *Exciting Sources*

In *IRAS* Point Source Catalog (Joint *IRAS* Science Working Group 1988) this region contains only IRAS 11101−5829. The position of this source is very close to that of HH 136 knot J, the difference being 0ˢ2 or 2″ in right ascension and 2″ in declination; the *IRAS* error ellipse is 5″ by 19″ in P.A. = 132°. But, which of the two HH objects is excited by IRAS 11101−5829? Our answer is HH 135 rather than HH 136 despite the above fact. The reason is that, as discussed in the preceding subsection, the velocity structure of HH 136 shows a tilt from the negative value in the northeastern part to the predominantly positive value in the southwestern part; this indicates that the exciting source of HH 136 must be located around its center, not around knot J. Also the morpholoy of HH 135 and 136 supports this interpretation; the bow shock structure of HH 135 points back to the source, while the bow of HH 136 knot B does not. Then, the flow of HH 135 lies in the direction of P.A. = 40°. On the other hand, the general morphology of HH 136 is elongated in P.A. = 33°, which must also manifest its flow direction.

This *IRAS* source is very bright with the observed flux densities 9.00 Jy (12 μm), 130.35 Jy (25 μm), 618.19 Jy (60 μm), and 750.21 Jy (100 μm). Using the distance of 2.7 kpc and the correction factor (according to Myers et al. 1987) for a wavelength range longer than 100 μm, we obtain $1.39 \times 10^4 L_\odot$ as the *IRAS* luminosity of IRAS 11101−5829. This is equivalent to the luminosity of a B0.5 ZAMS star and is almost as high as that ($1.55 \times 10^4 L_\odot$) of the HH 80/81 energy source which is by far the most luminous among the HH exciting sources known so far (Cohen & Schwartz 1987; Cohen 1990), the third being Z CMa ($\sim 3500 L_\odot$; Poetzel et al. 1989); we exclude the post–main-sequence object OH 0739−14. The *IRAS* colors of the source are $\log f_{12}/f_{25} = -1.16$ and $\log f_{25}/f_{60} = -0.676$. These colors place it, on the *IRAS* two-color diagram, to the lower left of the T Tauri box defined by Beichman et al. (1986). According to Fukui et al. (1992), sources located in this region and having high luminosities are very likely to have an energetic molecular outflow (see their Figs. 9 and 10).

Then, what excites HH 136? On Figures 4*b* and 5*d* we find that around knots D and E, which are located near the center of HH 136, the Hα emission is very strong and has both the blueshifted and redshifted wings; the Hα enhancement is apparent also in the low-dispersion spectrum of this region (see Fig. 3c), which shows strong continuum as well. These facts indicate that the energy source of HH 136 is probably located close to knots D or E.

Unfortunately in both the low- and high-dispersion spectroscopy the slit passed between knots D and E. Therefore from our slit spectroscopy we cannot tell which knot is responsible for the intense Hα emission with the broad wings. However, our objective-prism Schmidt plates, although the scale is small, suggests that it is knot E which very bright in Hα and, therefore, is more likely as the exciting source of HH 136. From the fact that the image of its core on the CCD frames is practically stellar (see, in particular, Fig. 2*b*) and that the [N II] 6548 and 6584 Å lines are very weak in the high-dispersion data (Figs. 4*b* and 5*d*), the core is suspected to be an emission-line star rather than an HH nebulosity. Presumably, it may be again an energetic source, although no *IRAS* point source is found coinciding with it, however.

The low-dispersion spectrum of HH 136 knots D/E displayed in Figure 4*c* has a strong continuum. It also shows Fe II permitted lines at 4924 Å and probably 5018 Å and 5169 Å, all of the multiplet 42, in emission. These lines are thought to originate from the stellar knot E rather than from the nebular knot D, since the 4924 Å line is as strong as [O III] 4959 Å (the Fe II permitted lines in HH 135 and HH 136 knot B are presumably of nebular origin, because the scattered light continua are not strong in these cases). Cohen, Dopita, & Schwartz (1986) found Fe II emission lines including the aboves in the scattered light components of some HH objects and argued that this provides evidence for the T Tauri nature of their exciting stars. But in the case of HH 136 the exciting source does not appear to be a T Tauri star for two reasons. First, Figure 3*c* shows that the continuum is not redward-rising but flat. Second, no enhancement of the H and K emission lines is found there. The presence of the above Fe II permitted lines may, however, suggest a sort of chromospheric activity of the source.

As for the P Cygni–like Hα profile found in the southwestern region of HH 136 (see § 4.2), the velocity of the Hα absorption core is -20, -16, and -21 km s^{-1} for knots D/E, G, and I, respectively. These are practically identical with the velocity of the background Hα emission (see the note to Table 4). This fact raises some doubt about the P Cygni profile interpretation. However, Hartigan & Graham (1987) observed a very similar Hα profile in R CrA, the probable exciting star of HH 104. In this case the absorption core velocity showed a very high variability, often making it almost undisplaced from the emission-line center. It is also noteworthy that in all of HH 136 knots D/E, G, and I, the [N II] 6584 Å line is weak relative to Hα (compare Figs. 5*a*–5*c* and 5*d*–5*f*) and does not have such a P Cygni–like profile. This indicates that reflected stellar emission from the exciting source contributes considerably to the Hα light of these knots. Thus it is concluded that the Hα profile is in fact of the P Cygni type, originating from the exciting source.

The velocity structure of the northeastern part of HH 136 is very interesting. Figures 4*b* and 5*b* to 5*d* (also see Table 4 and Figure 7 for quantitative data) show that the gas is accelerated as it moves northeastward away from knot E to knot B, where it makes the first bow shock and is rapidly decelerated. This behavior is similar to that of many HH objects having an optical jet discussed by Mundt, Brugel, and Bührke (1987). Strangely enough, however, HH 136 exhibits acceleration of the second stage after knot B until the gas attains as high a velocity as -270 km s^{-1} and forms the second bow shock at knot A. Contrary to the above, Figure 4*b* apparently indicates that the redshifted Hα gas is decelerated rather than accelerated around knot G. However, this is just a spurious appearance due to the decreasing intensity of the reflected light.

Two-staged bow shocks, similar to HH 136 knots A and B, are found in HH 46/47 (Hartigan, Raymond, & Meaburn 1990; Reipurth & Heathcote 1991), The 28 (Krautter 1986; Graham & Heyer 1988), and HH 111 (Reipurth 1989b). The most simple explanation of such structures is two intermittent outflows from a young stellar object. Another possibility is a magnetohydrodynamic effect. The MHD simulation of magnetized jets made by Uchida et al. (1992) and Todo et al. (1992) revealed that two types of Alfvénic shocks appear, among which the fast shock propagates much faster than the slow shock. Thus two-staged bow shocks are naturally explained by a single outflow event. This hypothesis will best be tested by proper motion measurements of the double bow shocks.

5. CONCLUSIONS

We have added two HH objects, HH 135 and HH 136, to the growing collection of this remarkable category of astrophysical objects. They are the most distant and most luminous HH objects known so far. They are located close by almost in a line and their flow directions are similar. Such an alignment is often the case in HH objects situated in the same molecular cloud (Reipurth 1989a; Ogura & Walsh 1991). So they partially overlap each other on the sky, which makes the whole region very complicated. HH 136 is huge (46″ or 0.60 pc long) and knotty, having double bow shocks. It probably represents a bipolar outflow inclined to the line of sight with both the positive and negative lobes observed. The energy source has tentatively been identified as its knot E. On the other hand, HH 135 corresponds to the negative velocity lobe of yet another outflow emanating from the extremely energetic *IRAS* source 11101−5829. The positive velocity lobe is hidden behind heavy obscuration. However, we cannot rule out the possibility that HH 136 is broken down further into two independent HH objects.

More detailed low- and high-dispersion spectroscopy, sampling each knot of HH 136, is required to better know their emission properties and velocity structures. Also very desirable is infrared imaging and polarimetric mapping of the whole region. Combination of these data will shed full light on the whole picture of these intricate and energetic objects.

We thank ATAC for giving us telescope time on the AAT. K. O. wishes to express his hearty thanks to the AAO for accepting him on a year's sabbatical leave from his home institute. He is indebted to the staff members of Kiso Observatory for their support in the measurements and data reductions. His special gratitude goes also to Cerro Tololo Inter-American Observatory for the telescope time as well as for the support during the observing runs.

REFERENCES

Beichman, C. A., Myers, P. C., Emerson, J. P., Harris, S., Mathieu, R., Benson, P. J., & Jennings, R. E. 1986, ApJ, 307, 337
Brand, J., Blitz, L., & Wouterloot, J. G. A. 1986, A&AS, 65, 537 (BBW)
Brugel, E. W., Böhm, K.-H., & Mannery, E. 1981, ApJ, 47, 117
Cohen, M. 1990, ApJ, 354, 701
Cohen, M., Dopita, M. A., & Schwartz, R. D. 1986, ApJ, 307, L21
Cohen, M., & Schwartz, R. D. 1987, ApJ, 316, 311
Fukui, Y., Iwata, T., Mizuno, A., Bally, J., & Lane, A. P. 1992, in Protostars and Planets III (Tucson: Univ. of Arizona Press), in press
Georgelin, Y. P., & Georgelin, Y. M. 1969, A&AS, 3, 1
Graham, J. A. 1968, AJ, 73, 17
Graham, J. A., & Elias, J. H. 1983, ApJ, 272, 615
Graham, J. A., & Heyer, M. H. 1988, PASP, 100, 1529
Gum, C. 1955, MmRAS, 67, 155
Hartigan, P., & Graham, J. A. 1987, AJ, 93, 913
Hartigan, P., Raymond, J., & Hartmann, L. 1987, ApJ, 316, 323
Hartigan, P., Raymond, J., & Meaburn, J. 1990, ApJ, 362, 624
Hartley, M., Manchester, R. N., Smith, R. M., Tritton, S. B., & Goss, W. M. 1986, A&AS, 68, 27
Herbig, G. H., & Jones, B. F. 1981, AJ, 86, 1232
Hoffleit, D. 1953, Harvard Ann., 119, No. 2
Joint *IRAS* Science Working Group 1988, The Point Source Catalog, Version 2 (Washington, DC: Government Printing Office)
Krautter, J. 1986, A&A, 161, 195
Mendoza, C. 1983, in IAU Symp. 103, Planetary Nebulae, ed. D. R. Flower (Dordrecht: Reidel), 143

Miller, J. S. 1968, ApJ, 154, L57
Moffat, A. F. J., & Vogt, N. 1975, A&AS, 20, 125
Mundt, R., Brugel, E. W., & Bührke, T. 1987, ApJ, 319, 275
Myers, P. C., Fuller, G. A., Mathieu, R. D., Beichman, C. A., Benson, P. J., Schild, R. E., & Emerson, J. P. 1987, ApJ, 319, 340
Ogura, K. 1990, PASP, 102, 1366
Ogura, K., & Walsh, J. R. 1991, AJ, 101, 185
Oke, J. B. 1974, ApJ, 27, 21
Paresce, F., & Nota, A. 1989, ApJ, 341, L83
Poetzel, R., Mundt, R., & Ray, T. P. 1989, A&A, 224, L13
Raymond, J. C. 1979, ApJS, 39, 1
Reipurth, B. 1989a, A&A, 220, 249
———. 1989b, Nature, 340, 12
———. 1989c, in Low Mass Star Formation and Pre-Main-Sequence Objects ed. B. Reipurth (Garching: ESO), 247
Reipurth, B., & Graham, J. A. 1988, A&A, 202, 219
Reipurth, B., & Heathcote, S. 1991, A&A, 246, 511
———. 1992, A&A, in press
Rodgers, A. W., Campbell, C. T., & Whiteoak, J. B. 1960, MNRAS, 121, 103
Seaton, M. J. 1979, MNRAS, 187, 73P
Shull, J. M., & McKee, C. F. 1979, ApJ, 227, 131
Solf, J., Böhm, K.-H., & Raga, A. 1988, ApJ, 334, 229
Steppe, H. 1977, A&AS, 27, 415
Sugitani, K., Fukui, Y., & Ogura, K. 1991, ApJS, 77, 59
Thackeray, A. D. 1967, MNRAS, 135, 51
Todo, Y., Uchida, Y., Sato, T., & Rosner, R. 1992, PASJ, 44, 245
Uchida, Y., Todo, Y., Rosner, R., & Shibata, K. 1992, PASJ, 44, 227